Method for evaluating the performance of railway crossing rails after long-term service

Zilong Wei, Alfredo Núñez, Anthonie Boogaard, Rolf Dollevoet, Zili Li*

Section of Railway Engineering, Faculty of Civil Engineering and Geosciences, Delft University of Technology, Stevinweg 1, 2628 CN, Delft, The Netherlands

ARTICLE INFO

ABSTRACT

In this paper, we present a method for evaluating the performance of railway crossing rails after long-term service. The method includes 1) 3D profile and hardness measurements; 2) finite element simulation of wheel/rail interaction; and 3) numerical prediction of rail degradation. We conducted a case study on a crossing that had been in service for several years. The results indicate that the crossing experienced a run-in process in the major traffic direction, manifested as a widening of the running band, an enlargement of the contact patch size, a decrease in contact stress and eventually a reduction in plastic deformation and wear. However, the wheel/rail interaction was exacerbated in the minor traffic direction which induced more severe plastic deformation and wear.

1. Introduction

The major function of railway crossings is to provide flexibility for railway operation, that is, allowing different tracks to intersect at the same level. Fig. 1 shows the main components of a railway crossing. At a crossing, a geometric discontinuity (i.e., a gap) is present by design between the wing rail and the crossing nose. High wheel/rail contact forces and undesired vibrations arise during the passage of vehicles over the discontinuity, and consequently crossings degrade much faster than ordinary plain tracks [1,2].

During long service periods, crossing rails may suffer from various types of defects, e.g., rolling contact fatigue (RCF; such as head checks, spalling [3] and cracks [4]) and accumulated plastic deformation and wear [5]. Crossings with severe RCF defects are easily identified, allowing for timely corrective maintenance actions (e.g., grinding and welding [6]). For a crossing without severe RCF defects, preventive maintenance is preferred but seldom taken even though the profile may have degraded significantly. For crossings in long-term service, the wheel/rail contact behavior may differ greatly from the nominal state, increasing the risk of sudden rail failure and even train derailment. Therefore, a better understanding of the performance of crossings that have experienced long-term service can help ensure that preventive maintenance is conducted in a timely manner and that the service life is extended.

The dynamic wheel/crossing interaction can be analyzed using the multi-body dynamics (MBD) method, the finite element (FE) method or some combination of the two. In the MBD model, the vehicle and track components are simplified as a combination of rigid or flexible bodies, springs and dampers [7–12]. The MBD method requires a limited number of degrees of freedom, and thus the computation procedure is fast. The MBD method is adept at analyzing the long-distance vehicle/track interaction to assess the stability and ride quality of vehicles. For the wheel/rail contact model, the normal and tangent problems are solved independently: usually, (semi- or multi-) Hertz springs for the normal contact and FASTSIM [13] for the tangent contact. These contact algorithms are restricted by half-space, linear elastic and steady state assumptions; therefore, their application at crossings is challenged by the complex contact geometry (e.g., conformal contact and large variations in the contact angle [14–18]), nonlinear material properties [19,20] and transient wheel/rail interaction [21].

To overcome the limitations of the MBD method in analyzing nonlinear materials and complex contact geometry, Nicklisch et al. [22] introduced an approach that combined the MBD and FE methods. In this approach, an MBD model was used to simulate vehicle dynamics and provide the input (e.g., contact force and contact position) for the FE modeling of rail degradation. A similar approach was also proposed in Ref. [23]. In these approaches, the prediction of plastic deformation relies on the normal contact parameters (e.g., pressure and contact patch size), while the tangent parameters (e.g., shear traction) essential for the precise analysis of rail degradation are absent. Moreover, the normal contact parameters are simulated using a simplified FE model involving only a quarter of the wheel/rail contact. Therefore, the

---

* Corresponding author.
E-mail addresses: z.wei@tudelft.nl (Z. Wei), A.A.NunezVicencio@tudelft.nl (A. Núñez), M.A.Boogaard@tudelft.nl (A. Boogaard), R.P.B.J.Dollevoet@tudelft.nl (R. Dollevoet), Z.Li@tudelft.nl (Z. Li).

Fig. 1. Main components of a railway crossing.

Fig. 2. Flowchart of the evaluation method.
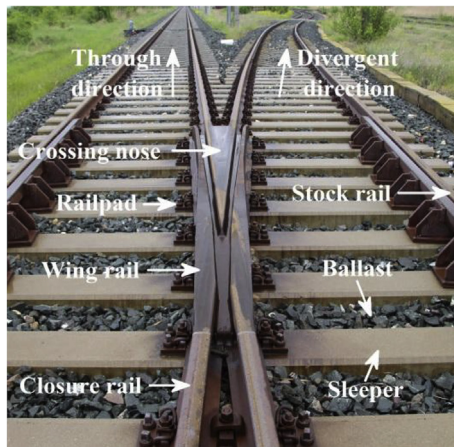
simulated contact patch always has an elliptical shape, which is often unrealistic for the complex geometry of crossings.

With the rapid development of computational power, the explicit FE method provides an alternative way to analyze dynamic wheel/rail interactions. The main advantage of the explicit FE method is that it allows a realistic adhesion-slip state in the contact patch to be obtained, because the non-differentiability of Coulomb's law [24] in the implicit FE method is avoided in a physical way [25].

Pletz et al. [26,27] developed an explicit FE model to simulate dynamic wheel/crossing interaction. In their model, a wheel with a constant load on the axle moves over a short piece of crossing rails (with a length of 3 m) suspended on a Winkler foundation. This model was further improved by Xin et al. [28], who extended the dimensions of the crossing model and included various missing components (e.g., the railpad and sleeper). The preceding two FE wheel/crossing models focus on the normal contact behavior and do not completely consider the tangent contact parameters (e.g., adhesion-slip state and shear traction). Thus, these models might not have satisfactory accuracy when analyzing crossing degradation. Recently, an explicit FE model was presented in Ref. [4] to examine the evolution of the wheel/crossing contact (in terms of the contact patch, adhesion-slip state, contact stresses and micro-slip) and to verify the simulated dynamic response (i.e., the major frequencies and energy distributions of axle box acceleration) via field measurements. However, the FE model presented in Ref. [4] was only demonstrated under nominal conditions, i.e., with nominal rail geometry and material properties, and the wheel/crossing contact behavior under various degraded conditions (in the presence of deformed crossing profiles and non-identical material properties) still remains unclear. To fill this gap, in this study, we integrate the FE model with other experimental and numerical approaches to analyze dynamic wheel/rail interaction at crossings after long service periods. Our results will help guide the preventive maintenance and extend the service life of crossing rails.

To model the degraded rails with actual geometry, a precise profile measurement is required. In the literature, crossing rails are commonly measured in two dimensions (2D) [5,6,23,29]. These 2D measurements suffer from the following issues. First, these measurements are taken at each cross section, and it is time-consuming to measure numerous cross sections. Therefore, adjacent cross sections are often spaced at large intervals (e.g., 50–300 mm [6,23,29]), and rail defects with short lengths may be missed or incompletely measured. Second, it is difficult to accurately correlate all the separately measured cross sections in the same coordinate system, which may introduce errors during numerical modeling. In this study, the crossing rails are measured in three dimensions (3D), so that the crossing profiles can be precisely captured in one measurement.

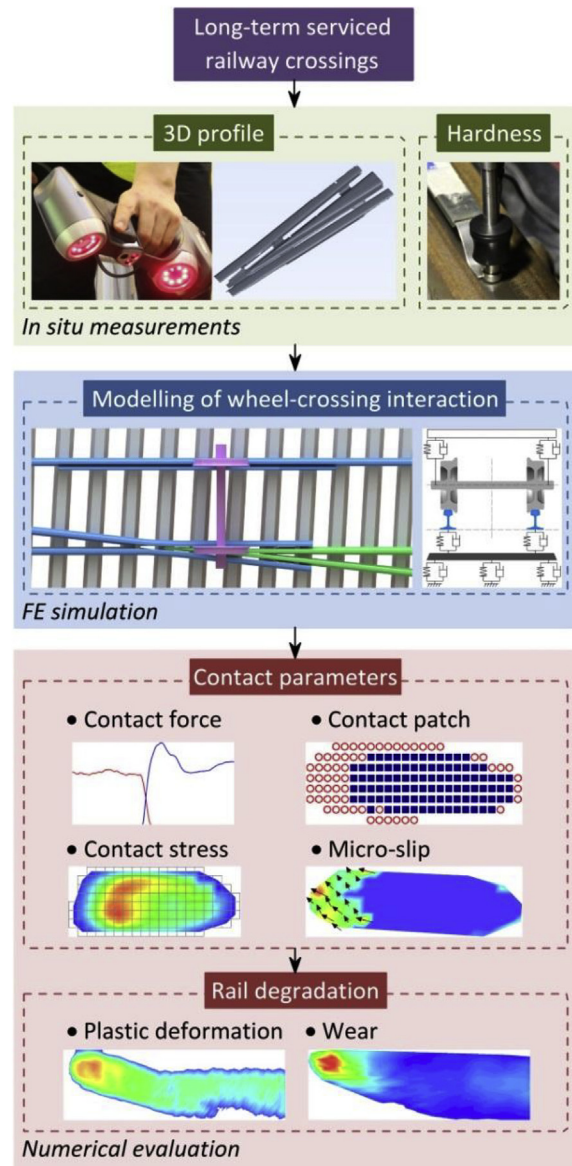In this study, we propose a method for evaluating the performance of crossing rails after long-term service. In the method, the 3D profiles and hardness of crossing rails are measured to provide the input for FE modeling of dynamic wheel/rail interaction, while the simulated contact behavior is used to predict the rail degradation due to wear and plastic deformation. The structure of this paper is arranged as follows. Section 2 describes the evaluating methodology, including in situ measurements and numerical simulations. Section 3 describes a case study on a railway crossing that had been serviced over many years. The results are discussed in Section 4, and the main conclusions are drawn in Section 5.

2. Method for evaluating crossing rails after long-term service periods

In this section, we describe a method for evaluating the performance of crossing rails after long-term service periods. The method is composed of 1) in situ 3D profile and hardness measurements, which serve as the input; 2) FE modeling of wheel/rail interaction to analyze the contact behavior; and 3) numerical prediction of rail degradation due to wear and plastic deformation. Fig. 2 shows a flowchart of the evaluation method.

2.1. In situ measurements

During long-term service, both the profile and the material behavior of crossing rails can degrade compared to nominal conditions. These degradations can be captured by 3D profile and hardness measurements.

The 3D rail profiles were measured using the laser-based apparatus HandyScan. During measurement, laser stripes are projected on the rail surface, while two cameras capture the reflected projections to extract the 3D data. The accuracy of the HandyScan device is as high as 0.03 mm in arbitrary directions, which is sufficient to capture slight changes in the crossing profiles.

A GE DynaMIC hardness tester was used for the in-situ hardness measurement. The hardness measurement was conducted on the surface of the crossing rails. Because the crossing rails may experience non-uniform hardening processes in the through and divergent directions, the rail hardness was measured along both directions. In this study, the measured hardness served as the input for the FE simulation of wheel/rail interaction and the prediction of rail degradation. In the FE simulation, the hardness H is converted to the yield strength σ_y using the following equation [30]:

$$\sigma_y = H/3 \times (0.1)^m \tag{1}$$

where m is the hardness coefficient.

2.2. FE modeling of wheel-rail interaction

The dynamic wheel/rail interaction at crossings is simulated using the commercial software ANSYS/LS-DYNA. In the FE model, the rails and sleepers are modeled with solid elements, while the railpads and ballast are modeled as linear springs and viscous dampers (Fig. 3). A railpad is composed of a uniform grid of 3 × 4 discretely distributed spring-damper pairs, and the ballast under each sleeper is composed of a uniform grid of 3 × 9 discretely distributed spring-damper pairs. The length of the crossing model is approximately 17.8 m, which includes 31 sleepers. To eliminate the disturbance of wave reflection at the boundaries, the FE model employs non-reflecting boundary conditions.

The wheelset is modeled with solid elements, and the car body and bogie are simplified as a lumped mass supported on the wheel axle by linear springs and viscous dampers. As the wheelset moves over the crossing, one wheel runs along the closure rail, the wing rail and then across the gap, impacting the crossing nose (see Fig. 3). The other wheel moves along the stock rail. The motion of the wheelset is defined as follows: 1) the longitudinal translation and the rotation about the y axis

are prescribed by specifying the translational velocity on both the carbody and wheelset, and specifying the angular velocity on the wheelset; 2) no constraints are specified on the lateral translation and the rotation about the z axis, and the wheelset is guided by the wheel-rail contact; and 3) the vertical translation and the rotation about the x axis can neither be prescribed nor fixed because they are a part of the dynamic response of the wheel-crossing interaction.

The calculation procedure is as follows: 1) the static equilibrium of the wheelset standing still on the crossing is computed using the implicit solver of ANSYS, and 2) dynamic wheel/rail interaction is simulated using the explicit solver of LS-DYNA to obtain kinematic and dynamic results such as nodal displacement and force. In the FE simulation, it is defined that the normal force is negative under compression, and thus the normal nodal force F_n is negative if a node locates within the wheel/rail contact patch. In addition, the nodal forces outside the contact patch are non-zero due to the inertia effect in a dynamic process. To minimize the disturbance of inertia effect, tolerances are required to obtain the physical distributions of the adhesion-slip state and contact patch. Therefore, the absolute value of the normal nodal force should satisfy the following expression if a node is in the contact patch:

$$|F_n| \geq \varepsilon_n \tag{2}$$

In addition, a node is located in the adhesion region if the following expression is true:

$$\mu|F_n| - |F_f| \geq \varepsilon_f \tag{3}$$

where F_f is the tangent nodal force. ε_n and ε_f are tolerances determined through the procedure shown in Fig. 4. Here, ε_n equals 0.15% of the maximum normal nodal force on the rail surface, and ε_f equals 0.4% of the maximum tangential force on the rail surface.

2.3. Prediction of rail degradation

The wheel/rail contact parameters obtained from the FE model are used to predict rail degradation due to wear and plastic deformation. Wear is the removal of material from the wheel/rail interface. In the literature, the frictional work method and the sliding method are commonly used to analyze the distribution of wear. In the frictional work method, the material loss depends on the energy dissipation [31–33], i.e., the work generated at the wheel/rail interface. For crossings after long-term service, the rails may experience non-identical hardening processes in different regions, which can affect the distribution of wear. Because the frictional work method does not directly
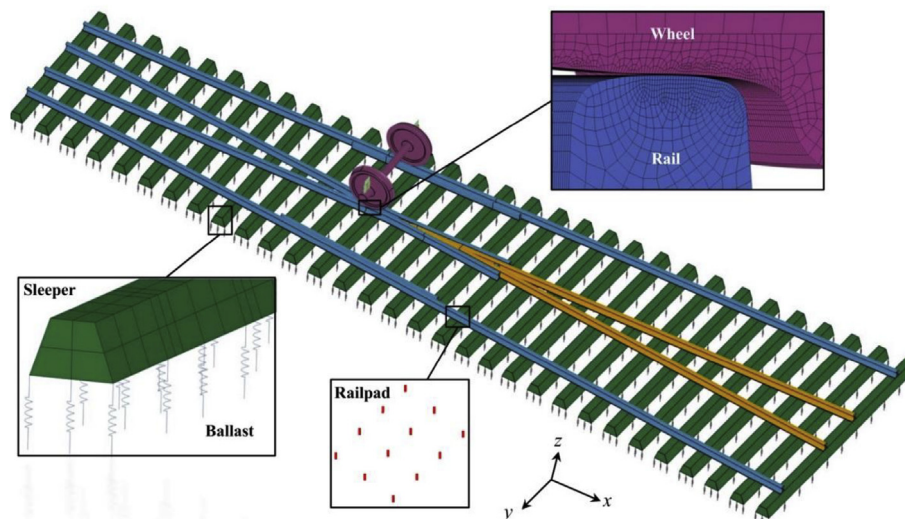

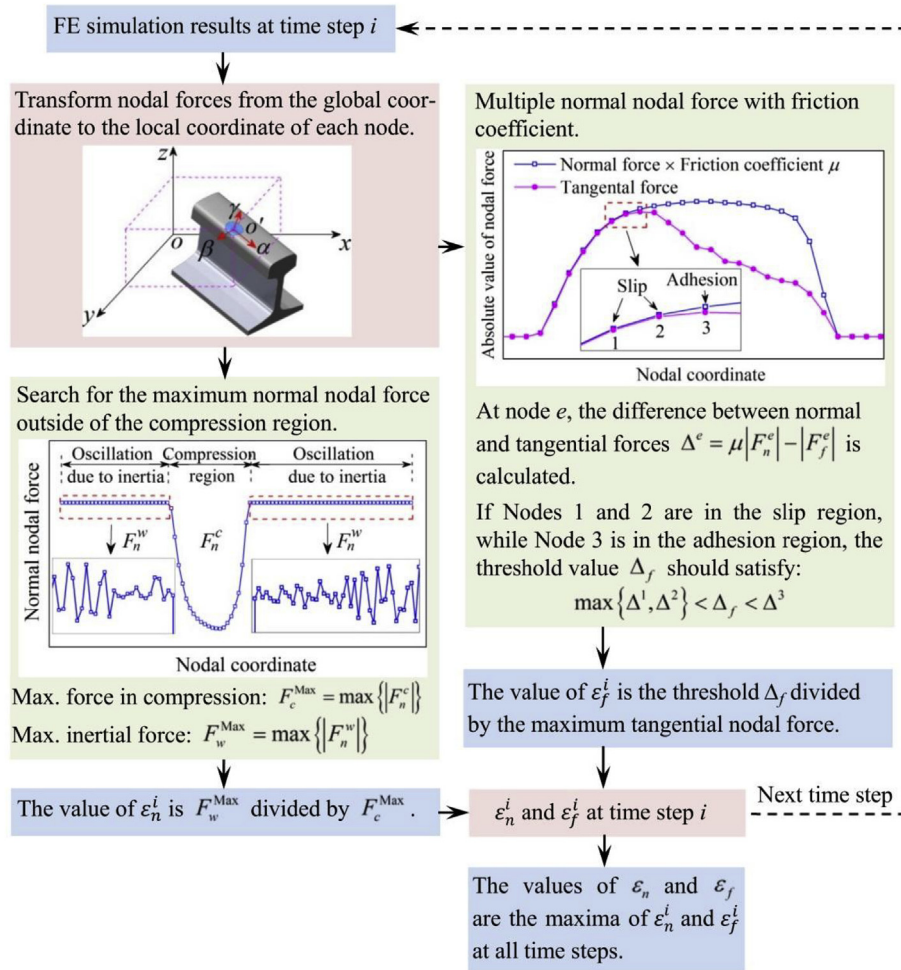**Fig. 3.** The FE model with close-ups of the mesh.

Fig. 4. Procedures for determining the tolerances ε_n and ε_f.

include the influence of non-identical hardening on wear, the sliding method is used in this study. The sliding method was initially proposed by Archard [34]. The wear volume V_{wear} can be expressed as follows:

$$V_{wear} = k_s \frac{F_n d}{H} \tag{4}$$

where d is the sliding distance, and H is the material hardness. The wear coefficient k_s is obtained from the wear chart [35] (Fig. 5). The wear chart is expected to relate the frictional contact to the wear distribution as generally as possible such that the wear chart is independent of the specific types of wheel and rail materials. In the literature, the wear chart has demonstrated its capability for different combinations of wheel and rail materials [5,36]. In future work, the
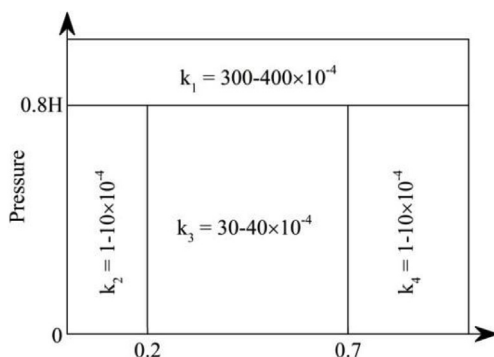

Fig. 5. Wear coefficient of Archard's model under dry conditions [35].

wear map can be calibrated via lab tests when the measured crossing is out of service and the rails are available for sampling. At a node of the rail surface, the wear depth Δz can then be calculated as follows [12]:

$$\Delta z = \frac{k_s}{H} \int_0^T ps \, dt = \frac{k_s}{H} \sum_{i=1}^n p_i s_i \Delta T \tag{5}$$

where p is the pressure, and s is the sliding velocity. ΔT is the time step for the output, and T is the duration of wheel/rail contact at the node equal to $n\Delta T$.

Plastic deformation originates from high contact stress; this deformation occurs when stress in a material exceeds a threshold value. In this study, the von Mises yield criterion is used to evaluate the plastic deformation, which is expressed as follows:

$$\sigma_v = \sqrt{\frac{1}{2}[(\sigma_{xx} - \sigma_{yy})^2 + (\sigma_{yy} - \sigma_{zz})^2 + (\sigma_{zz} - \sigma_{xx})^2 + 6(\sigma_{xy}^2 + \sigma_{yz}^2 + \sigma_{zx}^2)]}$$

$$\tag{6}$$

where σ_{xx}, σ_{yy} and σ_{zz} are the normal stresses; and σ_{xy}, σ_{yz} and σ_{zx} are the shear traction.

3. Case study: evaluating a crossing that has experienced long-term service

To evaluate the capability of the method proposed in Section 2, we conducted a case study on a Dutch railway crossing subjected to a long service period (see Fig. 6). The crossing is a 54E1-1:9 type with a UIC54 rail profile and a crossing angle of 1:9. The crossing rails are made of R260Mn rail material. During its 12-year service, the crossing profile
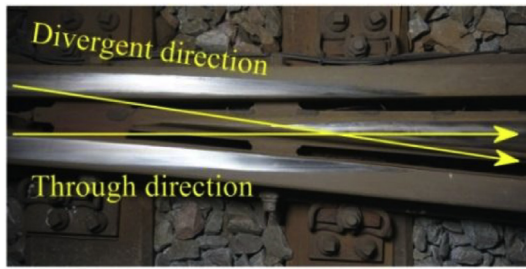
Fig. 6. The crossing subjected to long-term service in the case study.

changed significantly compared to the nominal condition, although no severe RCF defects were observed. According to statistics, 87% of the total traffic load was in the through moving direction and the rest occurred in the divergent direction. In both directions, the train operational speed is limited to 40 km/h.

3.1. Step 1: measuring the degradation status

3D profile and hardness measurements were conducted on the selected crossing. Fig. 7 shows the 3D crossing profile with a close-up of the measured data points. During the profile measurement, a three-dimensional Cartesian coordinate system was used, with the origin o at the tip of the crossing nose, and the x, y and z axes oriented in the longitudinal, lateral and vertical directions of the through moving direction, respectively.

The measured 3D crossing profile is composed of triangles (Fig. 7), and the vertexes of these triangles are the measured data points. In this study, these points serve as the input for FE modeling of degraded crossing profiles, and the procedure will be illustrated in Section 3.2.

As shown in Fig. 7, 12 cross sections were selected from the wing rail and crossing nose to gain insight into the change in profile from the nominal state to long-term service. Cross-sections W1 and W5 are along the centerlines of the wing rail, and cross-section N1 is along the centerline of the crossing nose; cross-sections W2-W4, W6-W8 and N2-N4 are perpendicular to the x axis.

Fig. 8 compares the crossing profile in the nominal state and after long-term service. Along the centerlines of the wing rail, the height difference between the two states reaches a maximum of 0.5 mm at W1 and 0.8 mm at W5. Due to the misalignment between the rolling direction of the wheelset and the centerlines of the wing rail (W1 and W5), the running band on the wing rail shrinks laterally toward the gauge side, as indicated by the shiny running band in Fig. 8. Consequently, no profile change could occur from $x=257$ mm along W1 and from $x=304$ mm along W5.
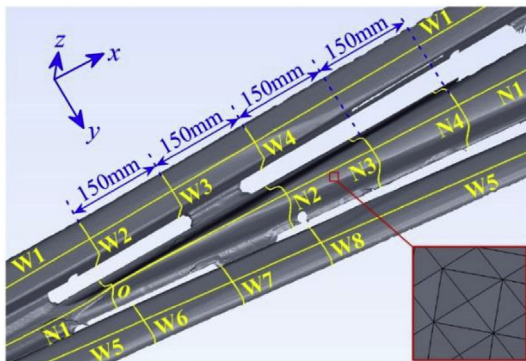

Fig. 7. Measured 3D crossing profile with a close-up of the data points (i.e., vertexes of triangles). Cross-sections W1 and W5 are along the centerlines of the wing rail and cross-section N1 is along the centerline of the crossing nose; cross-sections W2-W4, W6-W8 and N2-N4 are perpendicular to the x axis.

Regarding the lateral-vertical cross sections of the wing rail, the maximum height difference increases from 0.5 mm (W2) to 0.8 mm (W3) and then to 1.0 mm (W4). Meanwhile, the distance between the maximum height difference and the centerline W1 increases from W2 to W4, as shown in the first row of Fig. 8. Similar phenomena are also apparent in the second row of Fig. 8, where the maximum height difference increases from 0.8 mm (W6) to 1.0 mm (W7) and then to 1.3 mm (W8). On the wing rail, the running band becomes narrower along the rolling direction. This exacerbates the profile change and increasingly moves the maximal height difference laterally away from the centerlines (W1 and W5).

On the crossing nose, the profile change is significantly greater than on the wing rail. Along N1, the maximal height difference reaches 3.1 mm, which is at least 3 times higher than the height differences along W1 (0.5 mm) and W5 (0.8 mm). The maximum height difference at N2-N4 varies from 1.6 to 3.6 mm and the locations of these maxima move laterally away from the centerline N1 (see the third row of Fig. 8). Along N3 and N4, several small peaks in the height difference can be observed around the gauge corner, as denoted by the arrows marked "G". These peaks come with two-point contact, with the first contact occurring on the rail top and the second contact occurring at the gauge corner. The two-point contact can be either explicit or implicit (i.e., the second contact comes from the deformation at the first contact from the wheel load; see Fig. 6.7 in Ref. [15] and Fig. 5 in Ref. [37]) depending on the contact geometry and the moving trajectory of the wheels.

In the hardness measurement, a ruler made of soft paper was glued on the rails, and its edge coincided with the dashed yellow lines (see Fig. 9(a)). The hardness was measured every 10 mm along the edge of the ruler. Fig. 9(b) shows the hardness measured on the crossing that was measured every 10 mm along the through and divergent directions. For the purposes of comparison, the typical hardness of the nominal R260Mn material (i.e., 274 HV) is attached. At $x=200$–700 mm, the measured hardness along the through direction ranges from 302 to 389 HV, with the maximum occurring at $x=270$ mm. The hardness along the divergent direction ranges from 303 to 407 HV, with the maximum also occurring at 270 mm.

Because the hardness and yield strength of the nominal R260Mn rail material are known parameters, they can be used to determine the hardness coefficient of this material for Equation (1). The typical hardness and yield strength of the nominal material are 274 HV and 500 MPa. Thus, the coefficient m in Equation (1) can be determined as -0.74. By assuming the same hardness coefficient for nominal and degraded rail materials, we can estimate the yield strength of the degraded material from the measured hardness. For the case study crossing, the yield strength of the rails ranges from 553 to 712 MPa along the through direction and from 555 to 746 MPa along the divergent direction. In future work, the hardness coefficient of the degraded material can be calibrated via tensile tests when the crossing is out of service and the rails are available for sampling.

3.2. Step 2: characterizing wheel/rail contact behavior

This section simulates the passage of a wheelset over the long-term serviced crossing. The wheel profile is the nominal S1002. The average axle load is 16.8 tons and the stiffness and damping of the primary suspension are 880 kN/m and 4000 N/m, respectively [38]. The coordinate system used for the FE modeling is the same as for the 3D profile measurement. In the FE model, the profiles of the nominal crossing rails are taken from the drawings. The profiles of the degraded crossing rails are obtained from the 3D profile measurement, see Fig. 10(a). A bilinear elastoplastic material model is used to account for the plastic deformation of contact bodies. The density, Young's modulus, Poisson's ratio and tangent modulus of the wheel and rail are 7800 kg/m^3, 210 GPa, 0.3 and 21 GPa, respectively. The yield strength of the degraded rail materials is specified based on the hardness measurement, see Fig. 10(b). For the crossing, the stiffness and damping are
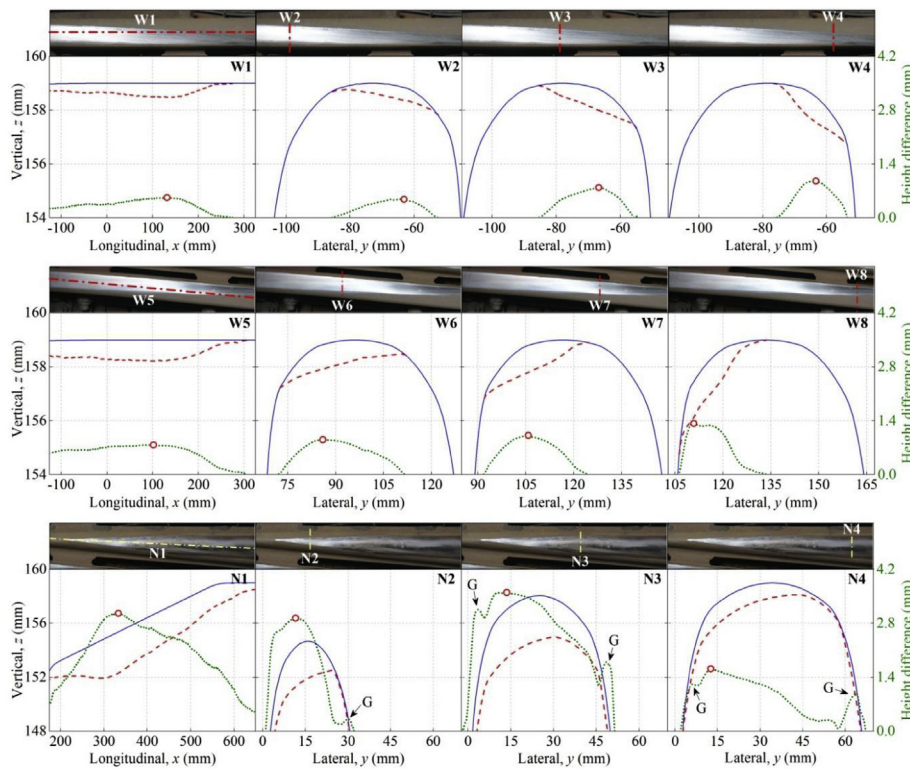
Fig. 8. Comparison of the crossing profile in the nominal state and after long-term service. The solid line (—) indicates the nominal rail profile taken from drawings, the dashed line (---) indicates the measured rail profile after long-term service and the dotted line (···) indicates the height difference between the two states. The dots (○) indicate the maximum height difference. The arrow marked G denotes the profile change due to flange contact.

1560 MN/m and 67.5 kN/m for a standard railpad, whereas the corresponding values of the ballast are 90 MN/m and 64 kN/m for a standard concrete sleeper [39]. The sleepers are treated as linear elastic bodies, with the Young's modulus, density and Poisson's ratio being 38 GPa, 2480 kg/m^3 and 0.2, respectively.

The frictional wheel/rail contact is defined by Coulomb's law, with the frictional coefficient being 0.4 for dry conditions [40]. At the wheel/rail interface, the minimum element size is set to 1×1 mm. In total, the FE model contains 478,553 elements. In the explicit FE simulation, the output time step ΔT is set to 4×10^{-5} s, at which the wheelset moves 0.44 mm.

For the nominal crossing, the rail profiles are symmetric with respect to the centerline N1. For the case study crossing (serviced over a long period of time), however, the measured profiles are no longer symmetric (see Fig. 8), resulting in different wheel/rail contact geometries for the through and divergent moving directions. To account for the influence of the asymmetric crossing profile on the wheel/rail contact behavior, both the through and divergent motions of the wheelset are simulated. In both directions, the train speed is set to

40 km/h.

Fig. 11 compares the normal contact force. The wheel starts to contact the nominal crossing nose at $x=230$ mm; the initial contact on the long-term serviced crossing nose shifts forward to $x=261$ mm in the through direction and to $x=246$ mm in the divergent direction. For the crossing after long-term service, the shift forward of the initial contact can be mainly attributed to the uneven crossing profile change (see Fig. 8); that is, a more severe change in the crossing nose relative to the wing rail should correspond to a greater shift in the initial contact. The maximum contact force is 97 kN for the nominal crossing; for the crossing after long-term service, this value increases to 104 kN in the through direction and 115 kN in the divergent direction. The increase in the contact force is also related to the more severe profile change in the crossing nose and thus the greater wheel/rail impact energy.

Fig. 12 shows the running band on the crossing nose. The figure displays the wheel/rail contact positions at the instants with the maximum contact force (i.e., t_1, t_2 and t_3 in Fig. 11). For the nominal crossing, the width of the running band, measured along the y axis, reaches 11 mm at $x=230$–600 mm. For the crossing after long-term
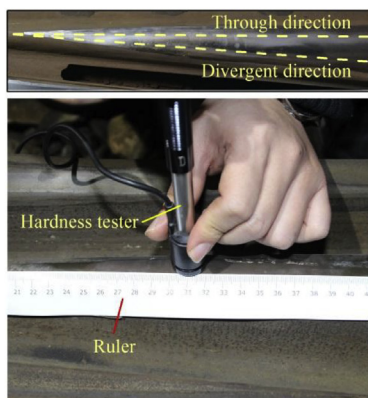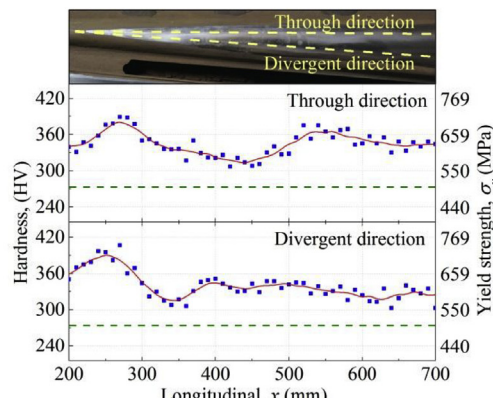
(a)   (b)

Fig. 9. In-situ hardness measurement. (a) Hardness tester, (b) hardness of crossing nose. The rectangles (■) indicate the hardness of the long-term serviced crossing rails measured every 10 mm along the two dashed lines; the solid lines (—) indicate the hardness of the long-term serviced crossing rails averaged for every three adjacent points; the dashed lines (---) indicate the hardness of the nominal crossing rails.
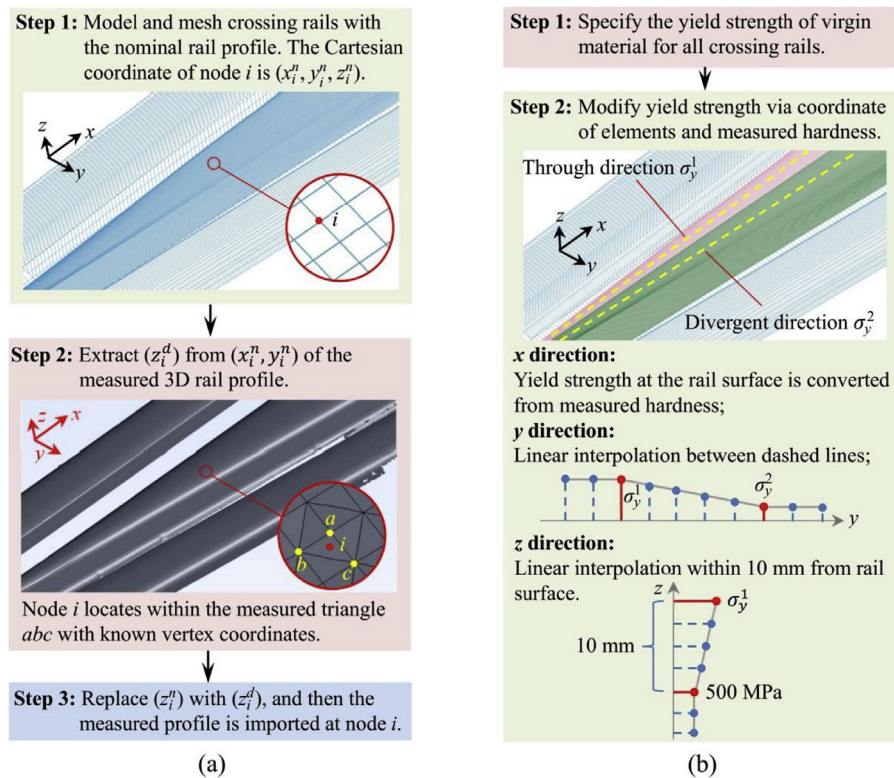
Fig. 10. Procedure for (a) modeling rail profiles via 3D profile measurement and (b) specifying the yield strength of rail materials via hardness measurement.
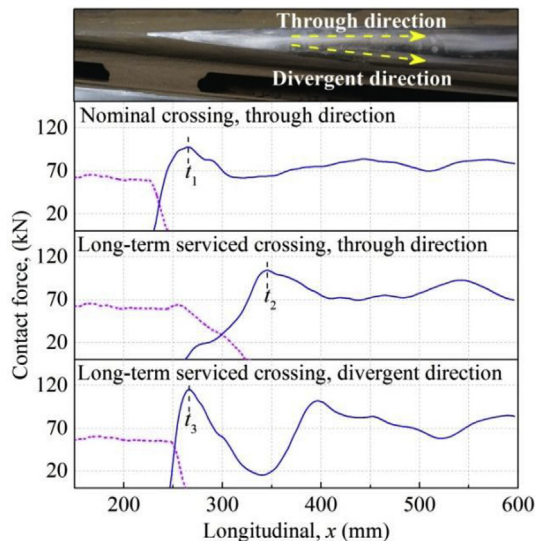

Fig. 11. Distribution of the normal contact force. t_1, t_2 and t_3 indicate the instants with the maximum normal contact force. The solid lines (—) indicate the contact force on the crossing nose, and the dashed lines (---) indicate the contact force on the wing rail.

service, the maximum band width increases to 14 mm in the through direction. The wider running band is due to the enlargement of the curvature radius of the lateral-vertical nose profile (see the inset plot in Fig. 12).

To facilitate the comparison of the running band between the through and divergent directions, the running band obtained in the divergent direction is projected to the through direction by mirroring across the centerline N1 (Fig. 7). The width of the running band is smaller for divergent motion on the serviced crossing (Fig. 12(c)) than for the other two scenarios (Fig. 12(a) and (b)). For example, the band

width in Fig. 12(c) is as small as 5 mm at x=230–350 mm, which is much lower than the values for through motion on the nominal crossing (8 mm in Fig. 12(a)) and the serviced crossing (14 mm in Fig. 12(b)). The narrower running band can be mainly attributed to the smaller curvature radius of the lateral-vertical crossing profile, as shown in the inset plot of Fig. 12(c).

Fig. 12 shows that the running band on both the nominal and the serviced crossings shifts laterally from the wheel flange root toward the wheel tread, i.e., from the rail gauge corner to the rail top. For the nominal crossing, the lateral shift is 6 mm at x=230–600 mm. For the crossing after long-term service, the lateral shift increases to 24 mm in the through direction and to 7 mm in the divergent direction. This deviation in the lateral shift mainly arises because of the non-identical and complex wheel/rail contact geometry (see Fig. 8). For through motion on the serviced crossing, the larger lateral shift in the running band may have negative effects on the ride quality of vehicles. This topic will be analyzed in future work.

To gain an insight into the wheel/crossing contact characteristics, Fig. 13 and Table 1 show the detailed contact behavior (adhesion-slip state, surface shear traction and micro-slip) at instants t_1, t_2 and t_3.

At the selected instants, the contact patch obtained for through motion on the crossing after long-term service has the greatest width (11 mm at t_2) and size (185 mm^2 at t_2). These values can be ascribed to the greater curvature radius of the crossing profile (see the inset plot in Fig. 12). Additionally, the wheel/rail contact position is closer to the wheel tread, where the curvature radius is also larger than at the flange root. By contrast, the contact patch for divergent motion on the crossing after long-term service has the smallest width (4 mm at t_3) and size (112 mm^2 at t_3). Therefore, the curvature radius of the crossing profile and the wheel/rail contact position are the crucial factors that determine the shape and size of the contact patch.

In the through direction, the magnitude of the normal contact force for the crossing after long-term service (104 kN at t_2) is 7% larger than for the nominal crossing (97 kN at t_1). However, the greater contact force value does not lead to greater contact stress values, because the
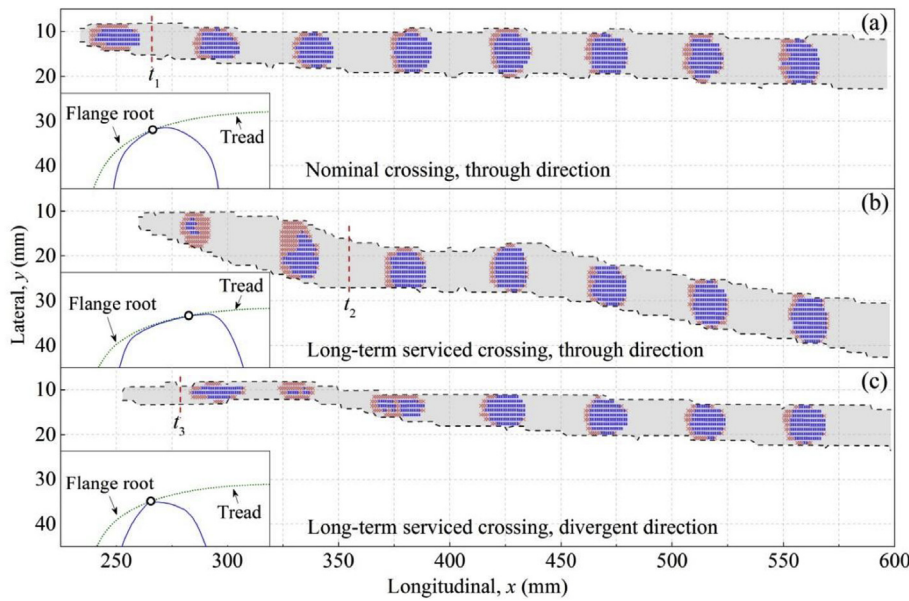
Fig. 12. Distribution of the running band. The dashed black lines (—) indicates the boundary of the band. The blue squares (■) and red exes (×) indicate the adhesion and slip regions, respectively. The inset plots show the wheel/rail contact positions at instants t_1, t_2 and t_3. The solid blue lines (—) and dotted green lines (···) indicate the crossing and wheel profiles, respectively. The open circles (○) in the inset plots indicate the contact patch centers. (For interpretation of the references to colour in this figure legend, the reader is referred to the Web version of this article.)

maxima of pressure and shear traction for the serviced crossing (1044 and 320 MPa at t_2) are reduced by 34% and 40% compared to the values for the nominal crossing (1583 and 529 MPa at t_1). The non-synchronized variations between the contact force and contact stress are caused by the greater growth of the contact patch size (30%, from 142 to 185 mm^2) relative to the contact force (7%, from 97 to 104 kN), which suppresses the magnitude of the contact stress. This phenomenon is a part of the run-in process, i.e., the adjustment in crossing profiles to achieve a stable relationship for the remainder of their service life. The run-in manifests as widening of the running band, enlargement of the contact patch size and eventually reduction of contact stress. For the serviced crossing, 87% of the total traffic loads occur in the through direction, and thus the crossing profiles are adapted to the major traffic loads in the through direction.

For the crossing after long-term service, the run-in occurred in the through direction. However, this process reduced the curvature radius of the crossing profile in the divergent direction, leading to a narrower running band, smaller contact patch size and thus greater contact stress. For example, the magnitudes of both pressure and shear traction (2691 and 918 MPa at t_3) are largest during the divergent motion on the serviced crossing. Therefore, run-in that is beneficial in the major traffic direction (the through direction in the case study) can exacerbate the wheel-rail contact in the minor traffic direction (the divergent direction

Table 1
Summary of contact parameters at instants t_1, t_2 and t_3.

Instant	Contact patch			Max. pressure (MPa)	Max. shear traction (MPa)	Max. micro-slip (mm/s)
	Length (mm)	Width (mm)	Area (mm^2)			
t_1	22	7	142	1583	529	146
t_2	18	11	185	1044	320	197
t_3	29	4	112	2691	918	201

in the case study).

Regarding the distribution of micro-slip, there is no micro-slip in the adhesion region (Fig. 13). In the slip region, the maximum micro-slip occurs near the rear edge of the contact patch. For the nominal crossing, the micro-slip reaches 146 mm/s at t_1. For the crossing after long-term service, the maximum micro-slip reaches 197 mm/s in the through direction at t_2 and 201 mm/s in the divergent direction at t_3. We note that the combination of high contact stress and micro-slip during divergent motion on the crossing after long-term service is expected to produce a high amount of wear, which will be examined in Section 3.3.

The analysis in Section 3.2 revealed the following wheel/rail contact characteristics during through motion (major traffic direction in
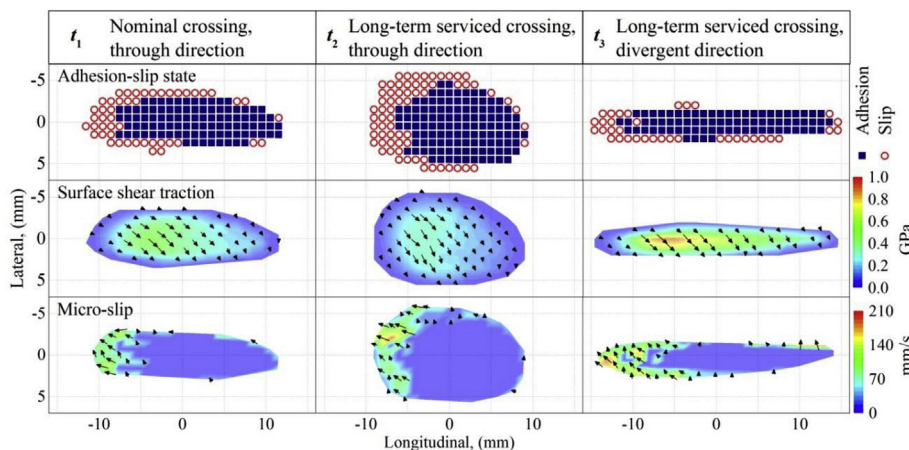

Fig. 13. Contact parameters at instants t_1, t_2 and t_3. The first row shows the adhesion-slip state, the second row shows the field of shear traction and the third row shows the field of micro-slip. The coordinates are adjusted for easier comparison of the results at different instants.

the case study) on the crossing after long-term service:

- The crossing experienced the run-in process, manifested as an increase in the curvature radius of the crossing profile, a widening of the running band and an enlargement of the contact patch size.
- Despite the slight increase in contact force, the magnitudes of pressure and shear traction were lower because of the run-in.
- The lateral shift in the running band from the wheel flange towards the wheel tread increased significantly.

During divergent motion on the crossing after long-term service (minor traffic direction in the case study), the following contact characteristics were observed:

- Both the width and size of the contact patch decreased because of the decrease in the curvature radius of the crossing profile and the lateral shift in the wheel/rail contact position.
- The combination of increased contact force and decreased contact patch size raised the magnitudes of both pressure and shear traction.

3.3. Step 3: evaluating the performance of crossing rails after long-term service

In this section, we use the wheel/rail contact parameters from the FE simulation to calculate the distribution of plastic deformation and wear. We use these results to assess the performance of the case study crossing rails relative to the nominal crossing.

Fig. 14(a) shows the distribution of the von Mises stress, which is calculated using Equation (6). For the nominal crossing, the von Mises stress exceeds the yield strength (500 MPa) from x=231 mm on, with the maximum of 947 MPa occurring at x=255 mm. For the crossing after long-term service, the maximum von Mises stress decreases by 26%–700 MPa in the through direction, and the region with plastic deformation shrinks to x=294–509 mm. The decrease in the von Mises stress and plastic deformation in the through direction is a benefit derived from the run-in. In the divergent direction, the von Mises stress for the crossing after long-term service reaches 2098 MPa at x=276 mm, which represents an increase of 122% compared to the nominal crossing. Because of the significantly greater von Mises stress, plastic deformation occurs from x=249 mm on.

Fig. 14(b) shows the field of the von Mises stress within the running band; both the trajectories of the contact patch center and the maximum von Mises stress are given. The two trajectories do not coincide with each other, and the lateral distance between them varies in the longitudinal direction. For the nominal crossing, the lateral distance

reaches 3.7 mm. For the crossing after long-term service, the maximum lateral distance reaches to 4.9 mm in the through direction and is reduced to 2.8 mm in the divergent direction. Because of the complex wheel/crossing contact geometry, the maximum von Mises stress may occur at any location within the running band. Thus, a wider running band is generally accompanied by a greater lateral distance value, and vice versa.

Fig. 15(a) shows the distribution of wear caused by one wheelset passage, which is calculated using Equation (5). For the nominal crossing, the wear depth caused by one wheel passage reaches its maximum of 1.9×10^{-6} mm at x=252 mm. For the crossing after long-term service, the maximum is reduced by 11% to 1.7×10^{-6} mm at x=277 mm in the through direction. The slight decrease in the wear depth is a benefit derived from the run-in process, which manifests as decreased pressure (Table 1) in addition to the increased hardness (Fig. 9(b)). In the divergent direction, the maximum wear depth on the crossing after long-term service is 11.2×10^{-6} mm at x=356 mm, which represents an increase of 489% compared to the nominal crossing. The sharp increase in the wear depth occurs because of the increase in both pressure and micro-slip (Table 1).

Fig. 15(b) shows the field of wear depth within the running band, including the trajectories of both the contact patch center and the maximum wear depth. The lateral distance between the two trajectories varies in the longitudinal direction, and a wider running band is generally accompanied by a greater lateral distance (4.0 mm, 4.5 mm and 3.8 mm for each of the three scenarios, respectively). This behavior, similar to that observed for the von Mises stress (Fig. 14(b)), is also related to the complex measured wheel/rail contact geometry. Comparing Figs. 15(b) and 14(b) shows that the trajectory of the maximum wear depth is not as smooth as the maximum von Mises stress, because the wear is a product of pressure and micro-slip and includes the irregularities in both components.

The analysis in Section 3.3 demonstrated the following characteristic distribution of plastic deformation and wear for the crossing after long-term service:

- In the major traffic direction (the through direction in the case study), the magnitudes of both the von Mises stress and wear depth decreased compared to those for the nominal crossing; this decrease is a benefit derived from the run-in process.
- In the minor traffic direction (the divergent direction in the case study), the magnitudes of both the von Mises stress and wear depth increased significantly.
- The trajectories of the maximum von Mises stress and wear depth did not coincide with the centerline of the running band. The lateral
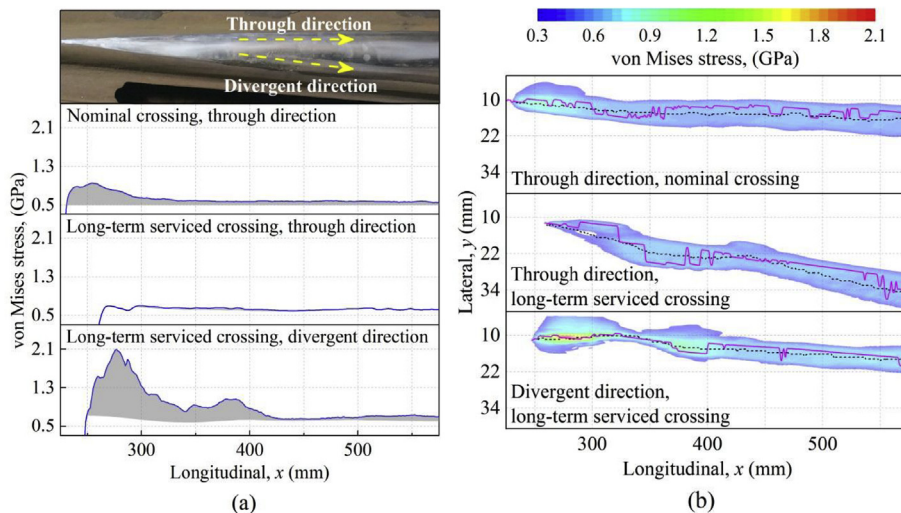

(a)   (b)

Fig. 14. Plastic deformation of the crossing nose. (a) Distribution of the von Mises stress. The shaded area indicates the region with plastic deformation; note that different scales are specified for each subplot. (b) Field of von Mises stress within the running band. The solid pink line (—) and the dashed black line (—) indicate the trajectories of the maximum von Mises stress and the contact patch center, respectively. (For interpretation of the references to colour in this figure legend, the reader is referred to the Web version of this article.)
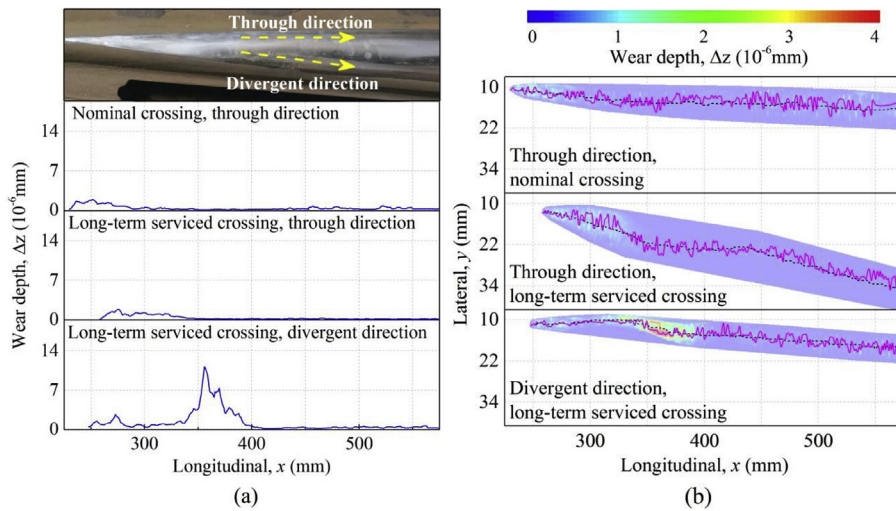
Fig. 15. Wear of the crossing nose. (a) Distribution of wear depth; note that different scales are specified for each subplot. (b) Field of wear depth within the running band. The solid pink line (—) and the dashed black line (—) indicate the trajectories of the maximum wear depth and the contact patch center, respectively. (For interpretation of the references to colour in this figure legend, the reader is referred to the Web version of this article.)

distance between them varied in the longitudinal direction, and a wider running band was generally accompanied by a greater lateral distance.

The results presented in Section 3 allow us to assess the performance of the crossing rails after long-term service. First, the crossing experienced a run-in process in the through direction (the major traffic direction in the case study); thus, rail degradation in this direction is slow and will likely not be a cause for urgent maintenance. However, the crossing rails suffered faster degradation in the divergent direction (minor traffic direction in the case study). To avoid a sudden failure of the rails in the minor traffic direction, preventive maintenance (e.g., grinding and repair welding) will be required to guarantee the safety of railway operation.

4. Discussion

4.1. Verifying numerical results with subsequent profile measurement

To demonstrate the capability of the proposed method, a second 3D profile measurement was performed 274 days after the first one. During the intervening period, 87% of the total traffic (1.06 million wheel cycles or 15.10 million gross tons) occurred in the through direction, whereas the rest occurred in the divergent direction. Fig. 16(a) shows the measured profile change of the crossing nose during the period. For comparison purposes, the simulated running bands are attached. In the figure, the regions with significant measured profile changes are almost enveloped by the simulated running bands. These regions are mainly distributed at approximately $x=250$–500 mm in the through direction and $x=250$–450 mm in the divergent direction, at which the simulated plastic deformation (Fig. 14) and wear depth (Fig. 15) also reach large values. This information demonstrates the capability of the proposed method to represent the characteristic rail degradation on the long-term serviced crossing. There are some small regions with clearly visible profile changes that remain outside the simulated running bands, probably because: 1) the FE model only employs the nominal wheel profile and nominal parameters of the track components, whereas the degradation of these components (e.g., hollow wheel tread and worn railpad) can affect the frictional wheel/rail contact; 2) the randomness of the wheel-rail interaction (e.g., hunting oscillation) is neglected in the analysis.

Fig. 16(b) shows spalling fatigue observed on the crossing nose in the divergent trajectory. In general, spalling is associated with high contact stresses in the material. In the numerical analysis, the contact stresses in the divergent direction were significantly higher than those in the through direction (Fig. 14), indicating that spalling has a greater
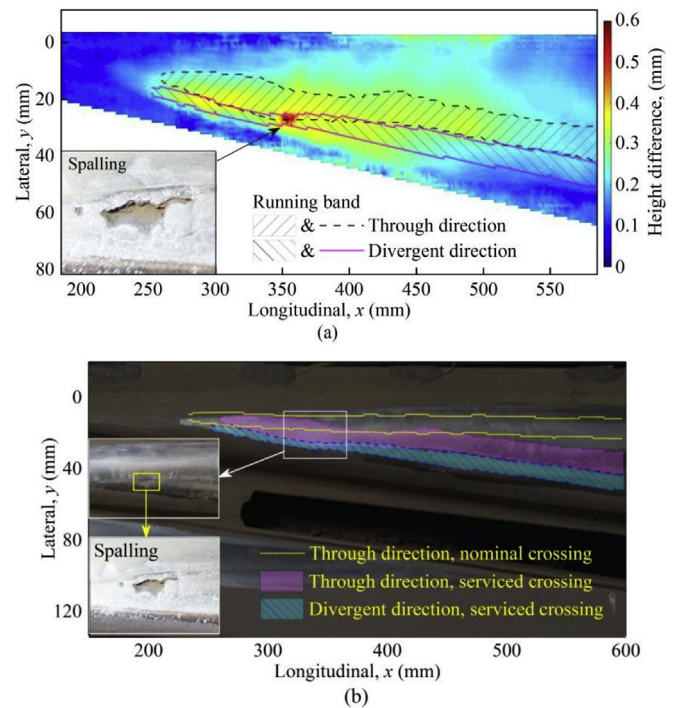

Fig. 16. (A) Measured profile change of the crossing nose during 274-day usage. (b) Spalling observed in the divergent trajectory of the crossing nose.

chance of growing in the divergent direction. Reasonable agreement was achieved between the in-situ observations and numerical simulations.

4.2. Criteria for guiding the preventive maintenance

The spalling fatigue in Fig. 16 would have a smaller chance of presence if maintenance actions (e.g., grinding and welding) are conducted in a timely manner. Proper criteria should be specified to determine the maintenance strategy. In general, a high value of contact stresses in the material is more dangerous than a high value of wear because the former can induce not only plastic deformation but also rolling contact fatigue (e.g., spalling, head checks, and shelling). Since severe rolling contact fatigue may result in the sudden failure of the crossing rails, stricter criteria should be specified for contact stress.

In the divergent direction, the maxima of the von Mises stress and wear depth on the serviced crossing (Figs. 14 and 15) increased by

122% and 489% compared to the maxima on the nominal crossing (which serve as the baselines). To minimize the presence of rolling contact fatigue and slow down the plastic deformation, the criterion for the maximum von Mises stress is set to 2 times the baseline. In addition, the criterion for the maximum wear depth, which can be less strict, is set to 3 times the baseline. If the evaluation results exceed these criteria, preventive maintenance actions should be performed in a timely manner.

Note that the preceding criteria are specified for the crossing type of 54E1-1:9 at a train operational speed of 40 km/h. These criteria should be adjusted for different crossing types and operational conditions. For example, stricter criteria are generally required for higher train speeds to guarantee the safety of railway operation.

4.3. Extending the capability of the proposed method

In the present study, we analyzed the degradation of crossing rails during the passage of one wheelset. To investigate the rail degradation caused by the passage of a number of wheels, the following analysis should be performed in subsequent work: 1) analysis on the residual stress in the rail material; 2) regular measurement of rail hardness to correct the yield strength of the rail material; 3) profile measurement of wheels that run over the crossing; 4) statistics of axle load, train speed and moving direction, and prescribing them in the FE simulation.

In addition to crossing rails, other track components (e.g., ballast and sleeper) can also experience degradation during long-term usage. For example, the presence of void ballast, moving sleepers as well as worn fastenings and railpads exacerbate dynamic wheel-rail interaction and accelerate the failure of the track structure. In future work, the parameters of these track components will be derived via in-situ impact measurements [41,42] to obtain a more comprehensive evaluation of the condition of long-term serviced crossings.

5. Conclusions and further work

In the railway industry, systematic evaluation of the performance of crossing rails after long-term service is important so that timely preventive maintenance can be conducted and sudden failures of the track infrastructure can be avoided. In this paper, we propose a method for analyzing the dynamic wheel/rail interaction at crossings after a long-term service period. The method includes the following: 1) 3D profile and hardness measurements, which serve as the input; 2) FE simulation of wheel/rail interaction to extract the contact behavior; and 3) numerical prediction of rail degradation. We applied this method to a case study to assess its capability. The main conclusions from the case study are as follows:

- In the major traffic direction, the crossing rails experienced a run-in process after long-term service, which was manifested as widening of the running band, enlargement of the contact patch size and eventually a reduction in contact stress. The magnitude of micro-slip was greater for the crossing after long-term service, but its growth was not as significant as the decrease in shear traction; thus, the wear depth decreased.

- The run-in process occurred in the major traffic direction for the crossing after long-term service; however, it exacerbated the wheel/rail contact in the minor traffic direction by decreasing the curvature radius of the crossing profile. Consequently, the running band narrowed, the contact patch size decreased and the contact stress increased, eventually leading to significantly increased von Mises stress and wear depth. This information indicates the necessity of conducting preventive maintenance actions to guarantee the safety of railway operations.

References

[1] Nielsen JC, Lundén R, Johansson A, Vernersson T. Train-track interaction and mechanisms of irregular wear on wheel and rail surfaces. Veh Syst Dyn 2003;40:3–54.

[2] Eker OF, Camci F, Guclu A, Yilboga H, Sevkli M, Baskan S. A simple state-based prognostic model for railway turnout systems. IEEE Trans Ind Electron 2011;58:1718–26.

[3] Wiest M, Daves W, Fischer F, Ossberger H. Deformation and damage of a crossing nose due to wheel passages. Wear 2008;265:1431–8.

[4] Wei Z, Shen C, Li Z, Dollevoet R. Wheel–rail impact at crossings: relating dynamic frictional contact to degradation. J Comput Nonlinear Dynam 2017;12:041016.

[5] Wang P, Xu J, Xie K, Chen R. Numerical simulation of rail profiles evolution in the switch panel of a railway turnout. Wear 2016;366:105–15.

[6] Wan C, Markine V, Shevtsov I. Improvement of vehicle–turnout interaction by optimising the shape of crossing nose. Veh Syst Dyn 2014;52:1517–40.

[7] Andersson C, Dahlberg T. Wheel/rail impacts at a railway turnout crossing. Proc Inst Mech Eng - Part F J Rail Rapid Transit 1998;212:123–34.

[8] Shu X, Wilson N, Sasaoka C, Elkins J. Development of a real-time wheel/rail contact model in NUCARS® 1 and application to diamond crossing and turnout design simulations. Veh Syst Dyn 2006;44:251–60.

[9] Kassa E, Andersson C, Nielsen JC. Simulation of dynamic interaction between train and railway turnout. Veh Syst Dyn 2006;44:247–58.

[10] Alfi S, Bruni S. Mathematical modelling of train–turnout interaction. Veh Syst Dyn 2009;47:551–74.

[11] Sun YQ, Cole C, McClanachan M. The calculation of wheel impact force due to the interaction between vehicle and a turnout. Proc Inst Mech Eng - Part F J Rail Rapid Transit 2010;224:391–403.

[12] Nielsen JC, Pålsson BA, Torstensson PT. Switch panel design based on simulation of accumulated rail damage in a railway turnout. Wear 2016;366:241–8.

[13] Kalker JJ. Three-dimensional elastic bodies in rolling contact. Dordrecht, Netherlands: Kluwer; 1990.

[14] Li Z, Kalker J. The computation of wheel-rail conformal contact. Proceedings of the fourth world congress on computational mechanics. BuenosAires. 1998.

[15] Li Z. Wheel-rail rolling contact and its application to wear simulation. Delft, Netherlands: Delft University of Technology; 2002.

[16] Burgelman N, Li Z, Dollevoet R. A new rolling contact method applied to conformal contact and the train–turnout interaction. Wear 2014;321:94–105.

[17] Blanco-Lorenzo J, Santamaria J, Vadillo EG, Correa N. On the influence of conformity on wheel–rail rolling contact mechanics. Tribol Int 2016;103:647–67.

[18] Sichani MS, Enblom R, Berg M. A fast wheel–rail contact model for application to damage analysis in vehicle dynamics simulation. Wear 2016;366:123–30.

[19] Pun CL, Kan Q, Mutton PJ, Kang G, Yan W. An efficient computational approach to evaluate the ratcheting performance of rail steels under cyclic rolling contact in service. Int J Mech Sci 2015;101:214–26.

[20] Meli E, Magheri S, Malvezzi M. Development and implementation of a differential elastic wheel–rail contact model for multibody applications. Veh Syst Dyn 2011;49:969–1001.

[21] Yang Z, Li Z, Dollevoet R. Modelling of non-steady-state transition from single-point to two-point rolling contact. Tribol Int 2016;101:152–63.

[22] Nicklisch D, Kassa E, Nielsen J, Ekh M, Iwnicki S. Geometry and stiffness optimization for switches and crossings, and simulation of material degradation. Proc Inst Mech Eng - Part F J Rail Rapid Transit 2010;224:279–92.

[23] Johansson A, Pålsson B, Ekh M, Nielsen JC, Ander MK, Brouzoulis J, et al. Simulation of wheel–rail contact and damage in switches & crossings. Wear 2011;271:472–81.

[24] Wriggers P. Computational contact mechanics. Berlin, Germany: Springer; 2006.

[25] Zhao X, Li Z. The solution of frictional wheel–rail rolling contact with a 3D transient finite element model: validation and error analysis. Wear 2011;271:444–52.

[26] Pletz M, Daves W, Ossberger H. A wheel set/crossing model regarding impact, sliding and deformation-Explicit finite element approach. Wear 2012;294:446–56.

[27] Wiedorn J, Daves W, Ossberger U, Ossberger H, Pletz M. Simplified explicit finite element model for the impact of a wheel on a crossing–validation and parameter study. Tribol Int 2017;111:254–64.

[28] Xin L, Markine V, Shevtsov I. Numerical analysis of the dynamic interaction between wheel set and turnout crossing using the explicit finite element method. Veh Syst Dyn 2016;54:301–27.

[29] Kassa E, Nielsen JC. Dynamic interaction between train and railway turnout: full-scale field test and validation of simulation models. Veh Syst Dyn 2008;46:521–34.

[30] Cahoon J, Broughton W, Kutzak A. The determination of yield strength from hardness measurements. Metall Trans 1971;2:1979–83.

[31] Pearce T, Sherratt N. Prediction of wheel profile wear. Wear 1991;144:343–51.

[32] Zobory I. Prediction of wheel/rail profile wear. Veh Syst Dyn 1997;28:221–59.

[33] Li Z, Kalker JJ. Simulation of severe wheel-rail wear. Proceedings of the sixth international conference on computer aided design, manufacture and operation in the railway and other mass transit systems. 1998. p. 393–402.

[34] Archard J, Hirst W. The wear of metals under unlubricated conditions. Proc Roy Soc Lond: Math Phys Eng Sci: R Soc 1956:397–410.

[35] Jendel T. Prediction of wheel profile wear—comparisons with field measurements. Wear 2002;253:89–99.

[36] Ramalho A, Esteves M, Marta P. Friction and wear behaviour of rolling–sliding steel contacts. Wear 2013;302:1468–80.

[37] Dollevoet R, Li Z, Arias-Cuevas O. A method for the prediction of head checking initiation location and orientation under operational loading conditions. Proc Inst Mech Eng - Part F J Rail Rapid Transit 2010;224:369–74.

[38] Zhao X, Li Z, Liu J. Wheel–rail impact and the dynamic forces at discrete supports of rails in the presence of singular rail surface defects. Proc Inst Mech Eng - Part F J Rail Rapid Transit 2012;226:124–39.

[39] Oregui M, Li Z, Dollevoet R. An investigation into the modeling of railway fastening. Int J Mech Sci 2015;92:1–11.

[40] Areiza Y, Garcés S, Santa J, Vargas G, Toro A. Field measurement of coefficient of friction in rails using a hand-pushed tribometer. Tribol Int 2015;82:274–9.

[41] Knothe K, Wu Y. Receptance behaviour of railway track and subgrade. Arch Appl Mech 1998;68:457–70.

[42] Oregui M, Li Z, Dollevoet R. Identification of characteristic frequencies of damaged railway tracks using field hammer test measurements. Mech Syst Signal Process 2015;54:224–42.